[6]   GL03720

MICROFRACTURES IN ROCKS FROM TWO GEOTHERMAL AREAS

MICHAEL L. BATZLE and GENE SIMMONS

Department of Earth and Planetary Sciences, Massachusetts Institute of Technology, Cambridge, Mass. (USA)

Core samples from the Dunes, California, and Raft River, Idaho, geothermal areas show diagenesis superimposed on episodic fracturing and fracture sealing. The minerals that fill fractures show significant temporal variations. Sealed fractures can act as barriers to fluid flow. Sealed fractures often mark boundaries between regions of significantly different physical properties. The fracture porosities measured on several samples are less than 0.1%. This low value indicates that fractures are effectively sealed or that fracturing is confined to the relatively few large fractures visible within the samples. Fracture sealing and low fracture porosity imply that only the most recently formed fractures are open to fluids.

1. Introduction

A dynamic geothermal system responsible for the observed fracturing and hydrothermal alteration of sediments has been suggested by several workers, including Elders and Bird [1], Helgeson [2], Facca and Tonani [3], and Elder [4]. In the model, cold, dilute, meteoric water descends along one limb of a convecting cell and increases in temperature. As it does, it precipitates carbonates and sulfates and dissolves silica, K_2O, Na_2O, and varying amounts of other compounds. As the brine convects either upwards or laterally, along another limb of the cell, it cools and precipitates such minerals as quartz, chalcedony or silica, adularia, pyrite, and analcime. In this way, the system forms a self-sealing cap rock. This cap rock is brittle and subject to repeated fracturing. We suggest that the fractures contain information on the past histories and the current state of the system.

Cracks present in rocks from two geothermal areas, the Dunes, California, and Raft River, Idaho, were studied using recently developed techniques [5–7]. We have examined the fracture porosity, chemistry, and morphology. The standard petrographic microscope, when used with 100 μm thick "crack sections" shows fracture and mineral distributions and spatial relationships. The scanning electron microscope is used to get a detailed view of fracture morphology. The electron microprobe gives the fracture and interstitial chemical compositions and spatial variations in compositions. Differential strain analysis (DSA), based on high-precision measurements of linear strain as a function of pressure, allows the determination of both the total fracture porosity and anisotropy in fracture orientation or distribution.

The Dunes area is located 15 km north of the U.S.–Mexico border in the Salton Trough of southern California (see Fig. 1). The samples come from a 612-m test well. The rocks consist of terrigeneous detritus of the Colorado River Delta (see Fig. 2). These rocks range in texture from shales to arenites to conglomerates which probably represent lacustrine, deltaic and dune, and alluvial sedimentary environments respectively. The rocks range from friable, poorly compacted sands to highly indurated silicified sands. Extensive petrologic studies have been done on these rocks by Elders and Bird [1]. Four samples were obtained for our study from rocks that were both within silicified zones and extensively fractured.

The Raft River area is located in southern Idaho approximately 9 km north of the Idaho–Utah border and south of the Snake River plain. The samples come from a 435-m well. The lithology ranges from silty and argillaceous sandstones and conglomerates to sandy shales, siltstones and claystones. The rocks represent almost exclusively an alluvial depositional environment.
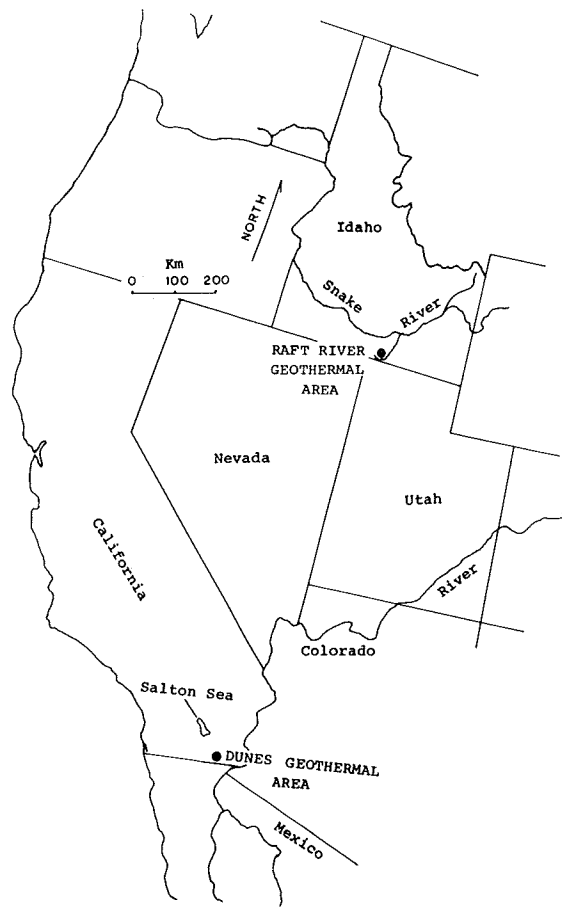
Fig. 1. Index map of sample locations.

areas both show diagenesis superimposed on episodic fracturing and fracture sealing. The chemistry of the fracture and interstitial mineralogy reflects the bulk composition of the surrounding rocks. The Dunes area rocks consist mostly of quartz and feldspathic arenites and wackes. The interstitial and fracture minerals are predominantly quartz and adularia. The Raft River area rocks consist of argillaceous sandstones and conglomerates and sandy claystones. The fracture minerals consist mostly of calcite, analcime, and, in one case, chlorite. The chemistry of the fluids can change significantly in time. In a Dunes area sample, the fluids change from quartz to adularia supersaturation and from reducing to oxidizing. In a Raft River area sample, the fluids change from calcite to analcime supersaturation and then to calcite undersaturation. The fracture porosities of the matrix of these rocks are surprisingly low, usually less than 0.1%. This value is extremely low and is most likely due to either the self-sealing nature of the system or the concentration of fracturing into relatively few large fractures.

In this paper, a fracture or crack is any place where a formerly continuous solid has been broken. Fractures are "healed" when the broken crystal lattice reforms across the fracture. Fractures are "sealed" when precipitated materials fill the void created by the fracture. A geothermal area is the location of unusually high heat flow or thermal gradient. A geothermal system refers to the entire physical and chemical makeup of a geothermal area, including rocks, fluids, and thermodynamic properties.

2. Observations and data

2.1 Fracture history, morphology, and mineralogy

In this section, we present the fracture history of each rock sample and the relationships among fracturing events. The relationships will also be determined between the fracturing and the local fluid properties as reflected in the fracture and interstitial mineralization. These histories are subsets of the history of each geothermal area as a whole. The results of the examination with the optical microscope, the scanning electron microscope (SEM), and the electron microprobe are presented graphically in Fig. 3. Only three samples, D 380, RR 1132, and RR 1107 will be described in
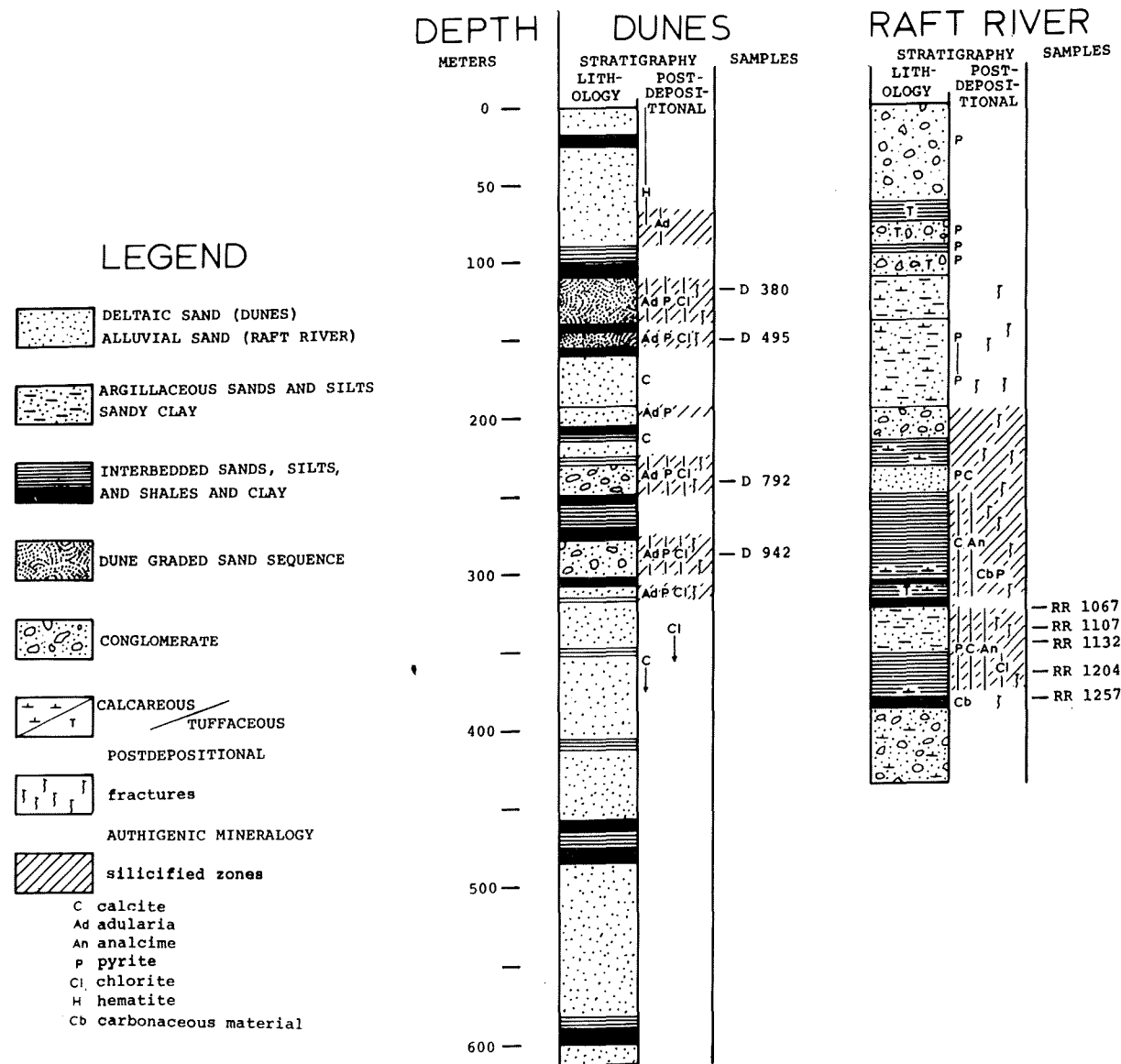
The rocks range from friable and pliable uncompacted sediments to rocks of moderate induration and silicification. Preliminary petrographic work is being done by Paul Williams and Harry Covington (of the U.S.G.S.). Five samples were obtained for our study from indurated rocks with fracturing.

The samples studied are *not* representative of the entire rock column. They were chosen specifically on the basis of their indurated nature and high degree of fracturing. Although our sample is biased for such purposes as determining average rock type or composition and measuring general physical properties, we believe that the set is an excellent one for the initial application of our techniques to the study of geothermal systems.

Rocks from the Dunes and Raft River geothermal

DEPTH | DUNES

METERS

RAFT RIVER

LEGEND

DELTAIC SAND (DUNES)
ALLUVIAL SAND (RAFT RIVER)

ARGILLACEOUS SANDS AND SILTS
SANDY CLAY

INTERBEDDED SANDS, SILTS,
AND SHALES AND CLAY

DUNE GRADED SAND SEQUENCE

CONGLOMERATE

CALCAREOUS
TUFFACEOUS

POSTDEPOSITIONAL

fractures

AUTHIGENIC MINERALOGY

silicified zones

C calcite
Ad adularia
An analcime
P pyrite
Cl chlorite
H hematite
Cb carbonaceous material

STRATIGRAPHY

LITH-OLOGY

POST-DEPOSITIONAL

SAMPLES

— D 380
— D 495
— D 792
— D 942

STRATIGRAPHY

LITH-OLOGY

POST-DEPOSITIONAL

SAMPLES

— RR 1067
— RR 1107
— RR 1132
— RR 1204
— RR 1257

Fig. 2. Stratigraphic setting. The Dunes area data is from Elders and Bird [1]. The Raft River data is compiled from Crosthwaite et al. [13].

detail as they exemplify best the relationships involved and the methods of investigation.

All the samples show compaction, alteration, and interstitial mineralization as the result of diagenesis. In the Dunes area rocks, quartz grains usually have developed quartz overgrowths and feldspar, clay, and lithic fragments commonly have either adularia or quartz overgrowths. Euhedral pyrite grains are common both interstitially and within lithic fragments. In the Raft River area rocks, large percentages of clay make the intergrain relations difficult to determine. Some of these rocks are moderately indurated by silici-
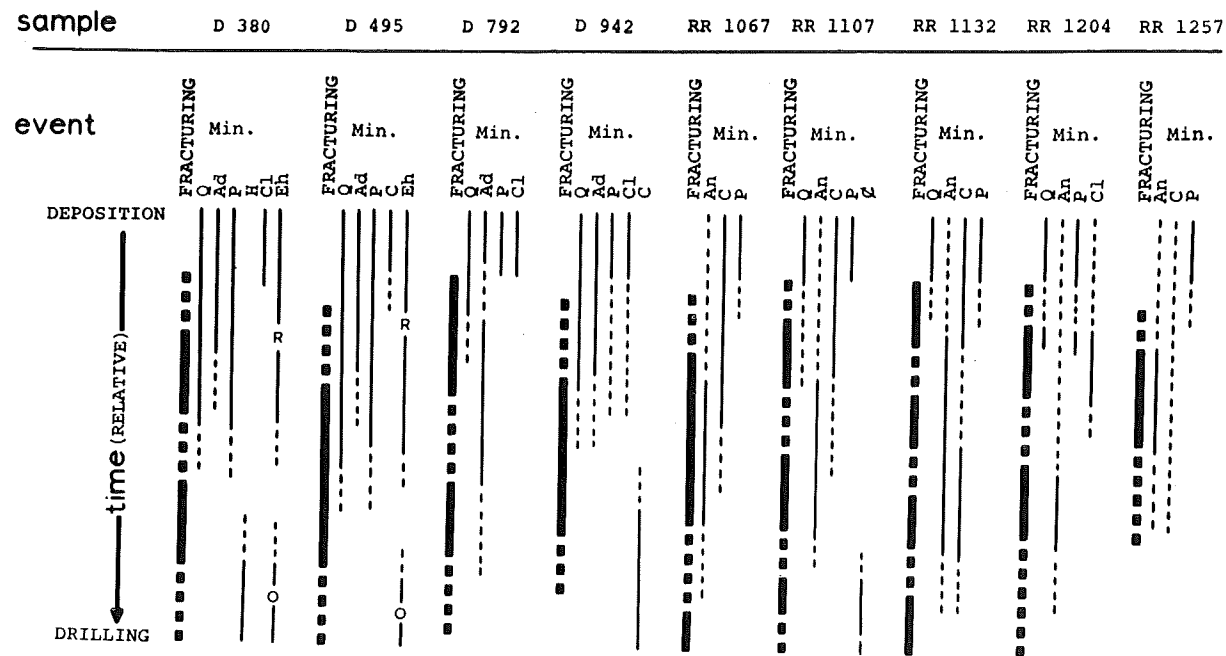
Fig. 3. Schematic fracture histories. The time scale is relative and indicates time relationships within each sample and not between samples. Dashed lines indicate that relationships are uncertain. "Min." represents precipitated minerals both interstitial and within fractures. "Eh" represents oxidation condition; R = pyrite stable (reducing conditions), O = pyrite oxidizing. "₵" represents conditions under which calcite was undersaturated with respect to the surrounding fluids.

Fracture and interstitial minerals: Q = quartz (or silica), Ad = adularia, An = analcime, P = pyrite, C = calcite or carbonate, Cl = chlorite, H = hematite.

fication and most of the rocks show interstitial growths of calcite and pyrite crystals (see Fig. 2).

Several fracture origins are possible in these sedimentary rocks. Grains may have been fractured at their source or in transport and deposition. Fractures can be produced in such processes of sampling and specimen preparation as drilling, shaping, cutting, and thin-sectioning. Of course, hammering on a specimen and dropping it can also produce fractures and should be avoided. The fractures of interest are those produced by the geothermal processes.

Several lines of evidence allow us to determine the temporal relationships among fractures. Overgrowths enclose older fractures but are transected by fractures younger than the overgrowth, as can be seen in Plate 1. Fractures also show cross-cutting relationships. Younger fractures often terminate on older ones. Progressive changes in fracture mineralogy can be used to date par-

ticular fractures. However, possible ambiguities can arise. Refracturing events can complicate the relations. New fractures often follow old lines of weakness. These lines of weakness can be old fractures or partially healed fractures as seen in Plate 2. Complex fracture shapes, usually at grain boundaries, can be misleading, particularly after refracturing events.

2.2. Sample D 380

Sample D 380 is a medium-grained, well-sorted feldspathic arenite. This sample is dull gray-red in color and is well indurated. An intergrown grain boundary texture results from almost all grains being enclosed by overgrowths. Sample D 380 shows several steeply dipping, open fractures to the unaided eye. These fractures are as wide as 1 mm.

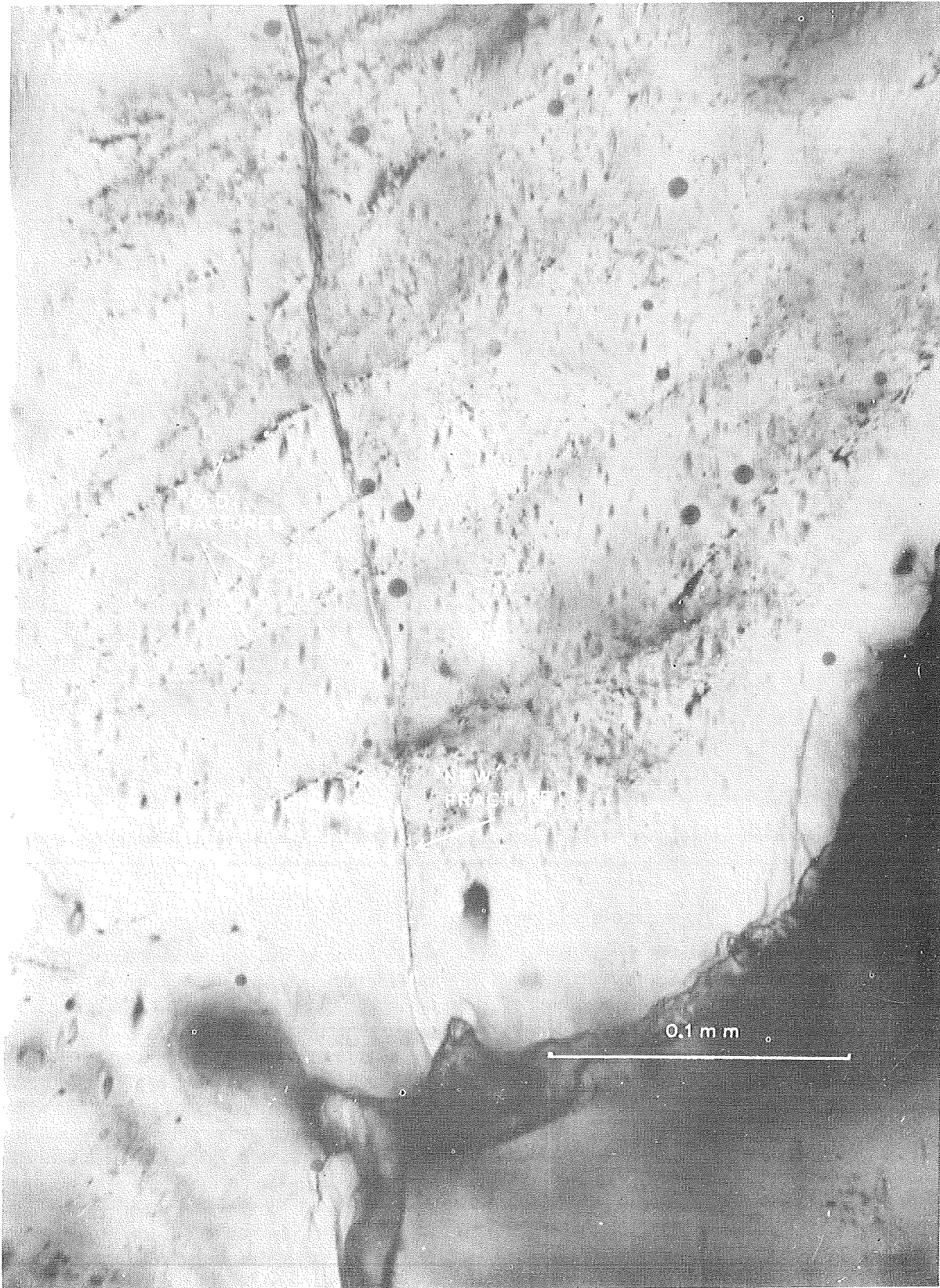Plate 3A and B contains evidence for four distinct

Plate 1. Fracture cutting relationships. Older fractures are surrounded by overgrowth. "New" fracture cuts overgrowth.
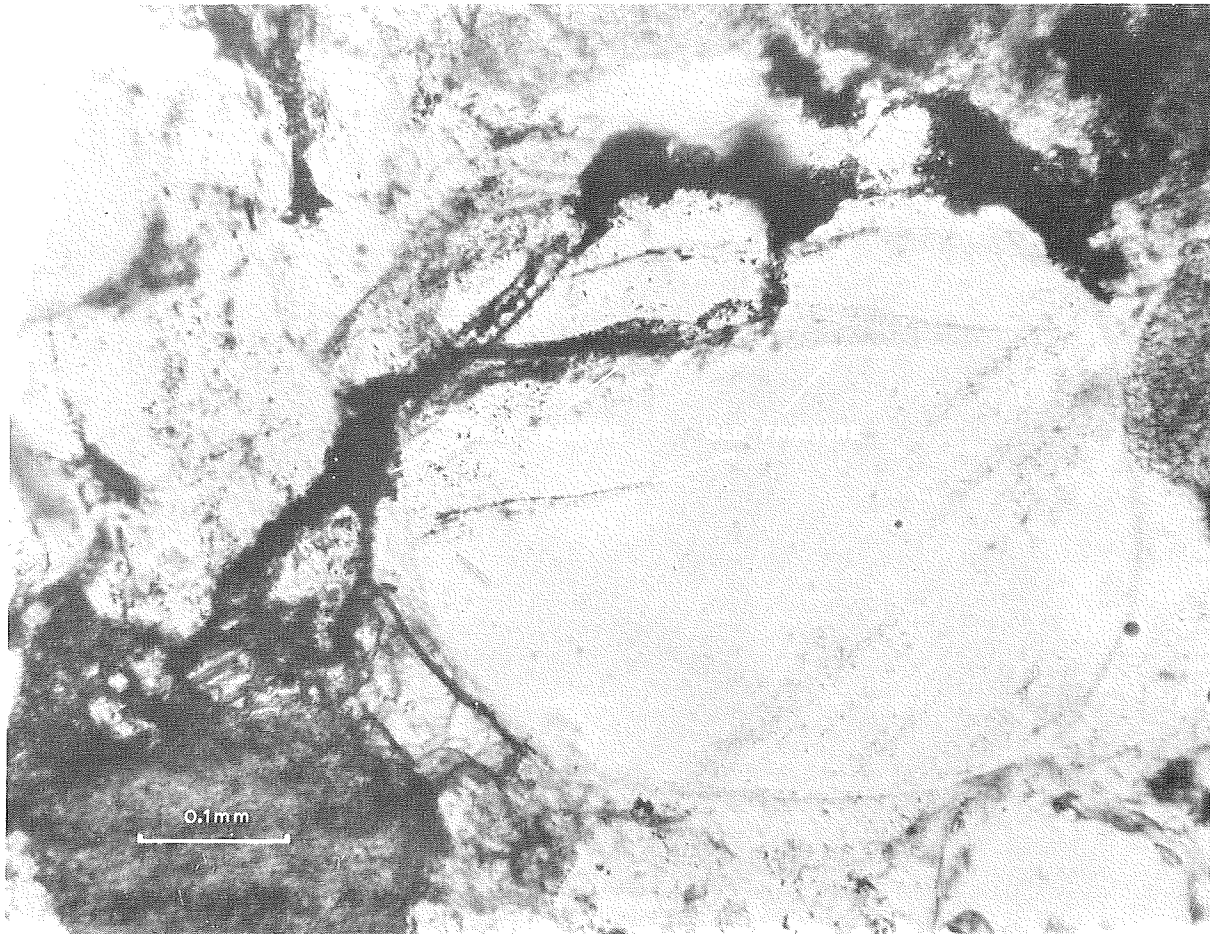
Plate 2. Refracturing. New fractures follow old lines of weaknesses. Here, healed fractures in the form of bubble planes are weaknesses.

episodes of fracturing. The episodes start with the major fracture *f1* and end with a minor fracture *f4*, possibly due to drilling. All but *f4* show same signs of healing or sealing by mineral precipitation. Examples of healing on fractures *f2* and *f3a* are shown at *healed f2* and *healed f3a* respectively. An example of fracture sealing by mineral precipitation is shown at *sealed f1*.

An ambiguity in the temporal relationships between fractures is seen along fractures *f2*, *f3b*, and *f3c*. Apparently, *f2* formed first, followed by *f3b* and *f3c*. The similarity of morphologies and merging near *D* of *f3b* and *f3c* indicates that they are the result of the same fracturing event. Fracture *f3c* terminates on fracture

f2 at location *K*. This termination indicates that *f3b* is younger than, or at least the same age as, *f2*. However, *f3b* and *f2* merge at *L*. Here at *L*, *f3b* most likely represents refracturing of *f2*.

The minerals sealing the major fracture *sealed f1* are mostly quartz with the addition of a few pyrite grains. Other fractures are either open or mineralized with quartz. The sharp, unetched nature of the fracture boundaries within quartz grains indicates that the fluids were always silica-saturated.

Sample D 380 shows the effects of time-varying fluid chemistry. The fluids in the rock were in the process of oxidizing pyrite. Both oxidized rims around
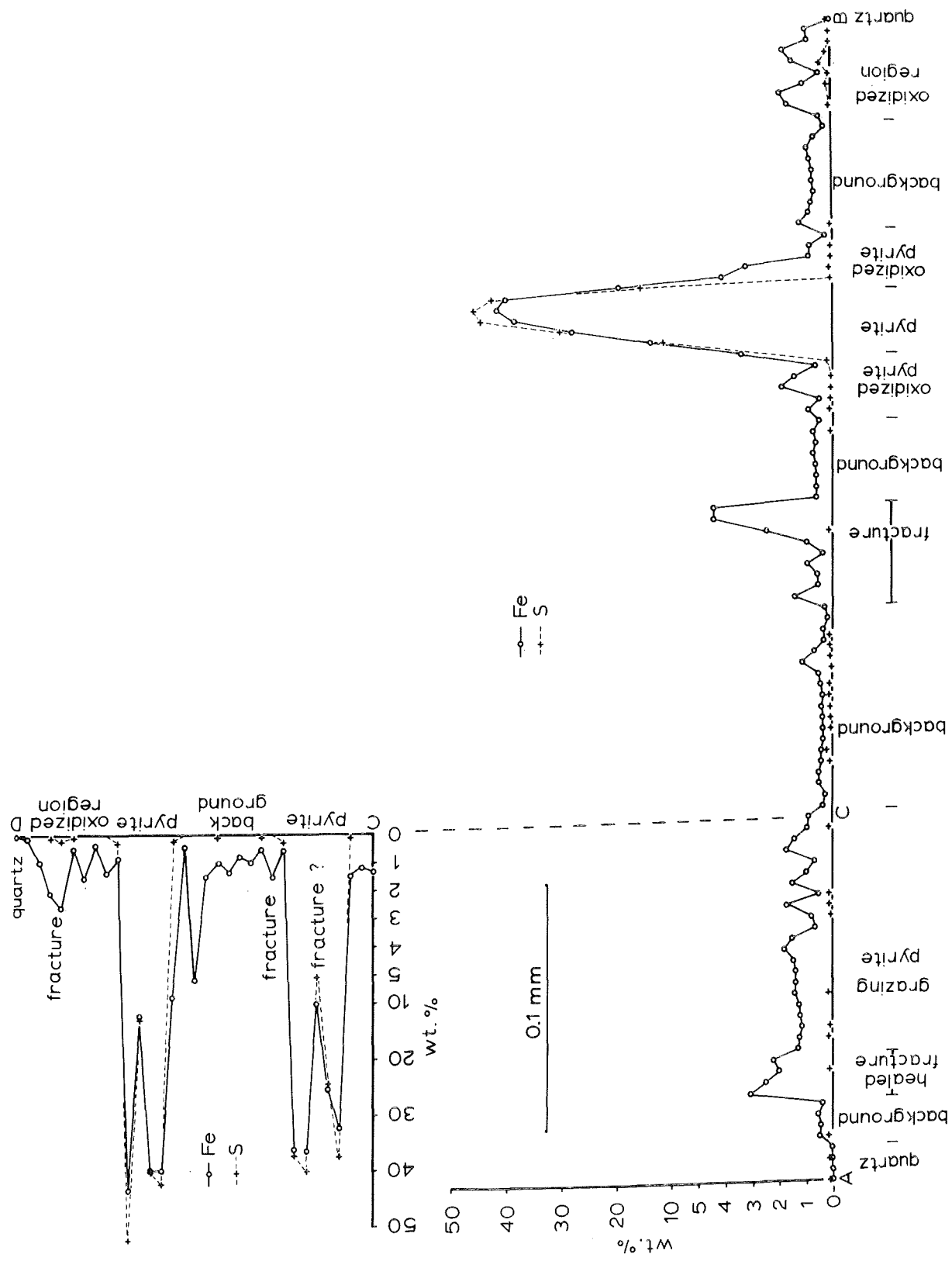
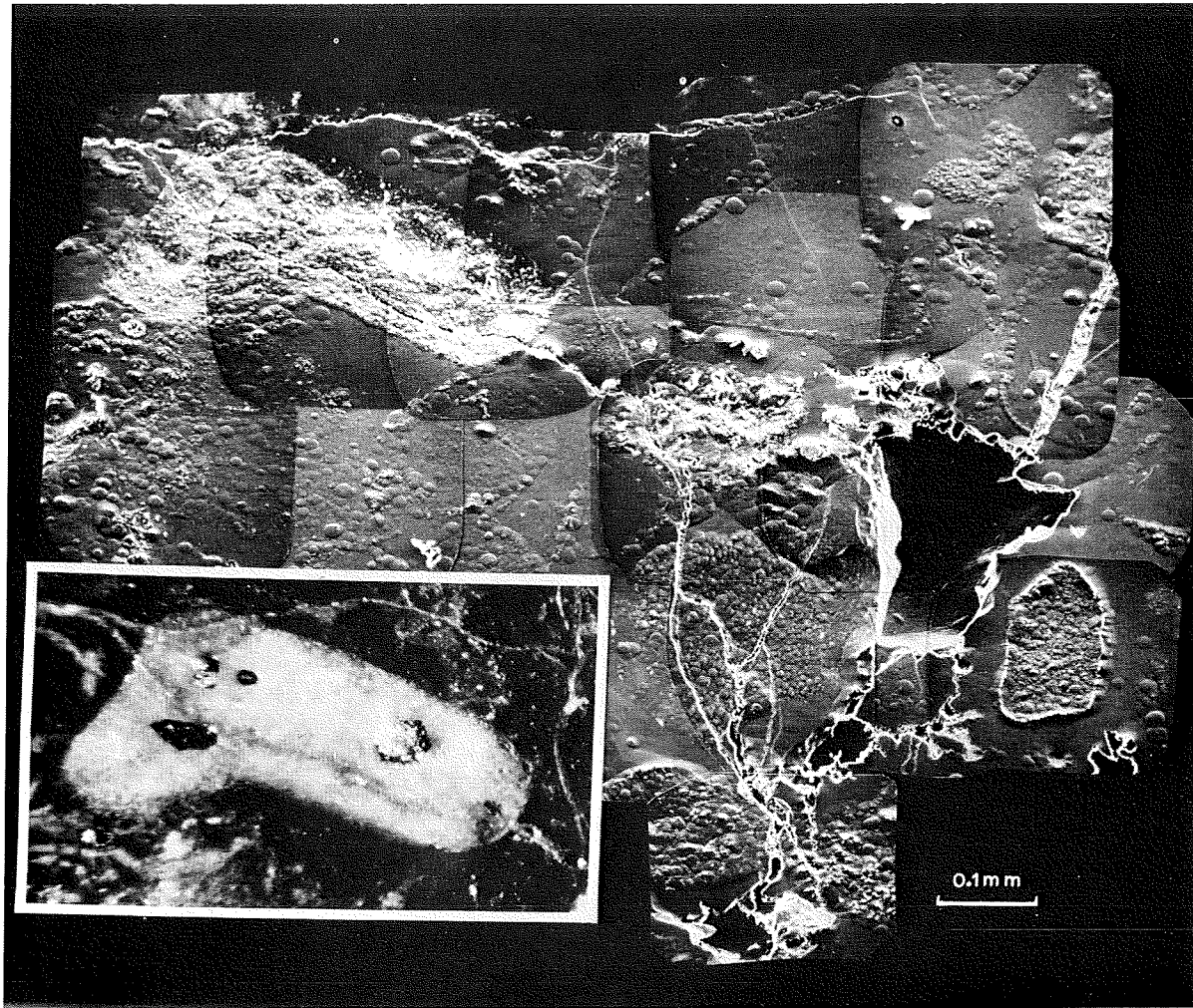Fig. 4. Sample D 380. Microprobe traverses $A-B$, $C-D$. See Plate 3.

Plate 3A. Sample D 380. Scanning electron photomicrograph mosaic of an area of fracture intersections. The hummocky topography is a result of milling the sample surface with ionized argon. See also Fig. 4. In the inset, the feldspar is viewed with an optical microscope using reflected light.

many pyrites and varying degrees of pyrite oxidation exist throughout the sample. At some locations within the major fracture $f1$, pyrite grains are almost completely altered to hematite. At other locations within this same fracture, unaltered euhedral pyrite grains still exist. Hence, fluid flow is restricted to specific sites within the fracture.

The progressive oxidation occurs in a particularly significant form within the altered clay ($A-B$, $C-D$). The oxidation reaction is poorly understood. Apparently, pyrite is oxidized to hematite and a highly soluble sulfate or hydrogen sulfate complex [8]. The sulfate is removed from the sample in solution. The hematite coats the pyrite grains and, more importantly, is distributed along the fractures. The active fractures, or fractures open to oxidizing fluids, appear as an abrupt rise in the iron background in microprobe analysis.

This correlation is seen in the microprobe traverse $A-B$ in Fig. 4. Proceeding from B to A there is an abrupt rise in the iron content when crossing the first
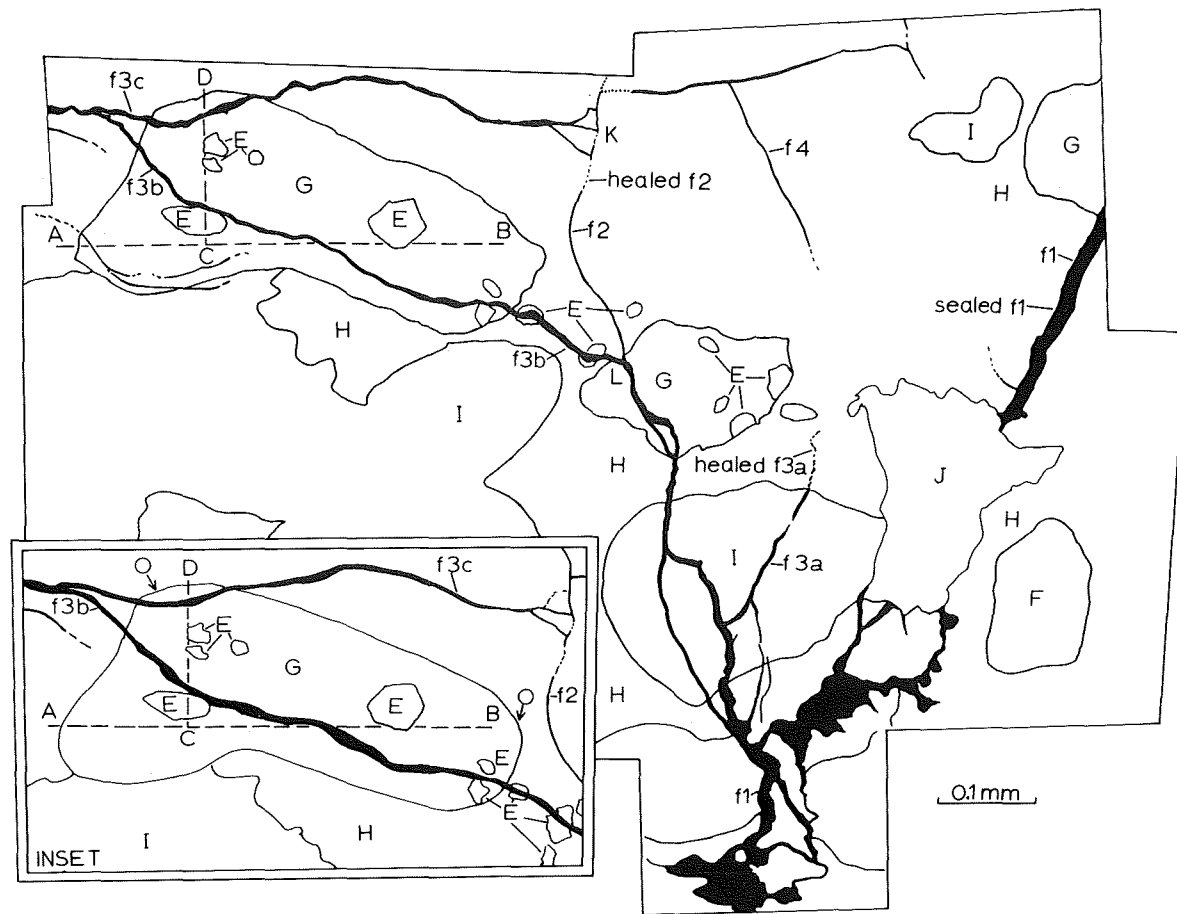
Plate 3B. Index sketch of the principle features of plate 3A. $A-B$, $C-D$ = microprobe traverse lines through altered feldspar; E = pyrite grains; F = lithic fragment; G = altered clay fragment; H = authigenic quartz overgrowth; I = interior of detrital quartz grain; J = void now filled with epoxy; K, L = fracture intersections; $f1$ to $f4$ = fractures (see text).

fracture $f3b$. The traverse then parallels the fracture for about 0.04 mm. This juxtaposition results in the gradual decrease in iron to the left side of the peak. Therefore, active fractures can be recognized on the basis of the local iron content. The iron in the fracture cannot be due to broken pyrite grains emplaced there during grinding because the sulfur content remains essentially zero within the fracture.

Zones of progressive oxidation can also be seen. These appear as shaded areas (brick red in color) in the clay as indicated in the inset of Plate 3. The $A-B$ traverse across the pyrite grain (E) shows a slight flaring only of the iron content which represents a coating of hematite. The pyrite near C in traverse $C-D$, how-

ever, shows no such flaring. Fracture $f3b$ crosses the traverse $C-D$ on the upper boundary of the pyrite grain near C. The fracture $f3b$ here only slightly increases the background iron content. The decrease in the iron and sulfur contents near the center of the pyrite grain may be due to a small "healed" fracture. The relative increase of iron with respect to sulfur indicates that both this healed fracture and $f3b$ are localized areas of oxidation. The presence of strong oxidation gradients within the feldspar ($A-B$, $C-D$) is interpreted to mean that oxidizing fluids are restricted to the vicinity of fractures.

In brief, the fracture history of sample D 380 is one of repeated fracturing events superimposed on time-

varying fluid chemistry. Fracturing occurred, followed by precipitation of quartz and pyrite. In turn, periods of fracturing and then oxidation followed. Varying degrees of oxidation show that, at any one time, different portions of the same fracture can be both open or closed to the circulating fluids.

2.3. Sample RR 1132

Sample RR 1132 is a gray-green, argillaceous, poorly sorted sandstone (see Fig. 2). Pyrite grains are visible throughout the sample. Bedding is indicated by several centimeter-wide dark bands with shallow dips. The high clay content makes observation by transmitted light impossible except for areas of translucent fracture mineralization.

In sample RR 1132, several sealed and unsealed fractures are visible to the unaided eye. The sample is divided by the fractures into two regions. One region is well indurated with siliceous cement and minor carbonate cement. The other region is friable and easily crumbles when handled. This division indicates that the sealed fractures have acted as effective boundaries to the circulating fluids responsible for the induration. Continuity of bedding across fractures indicates that there has been no significant movement along fractures.

SEM photomicrographs of an area of intersecting fractures are shown in Plates 4, 5, and 6. Five episodes of fracturing are indicated. The first to occur, fracture $f1$ in Plate 4, is now filled with calcite. The calcite tends to grow inward in small tablets perpendicular to
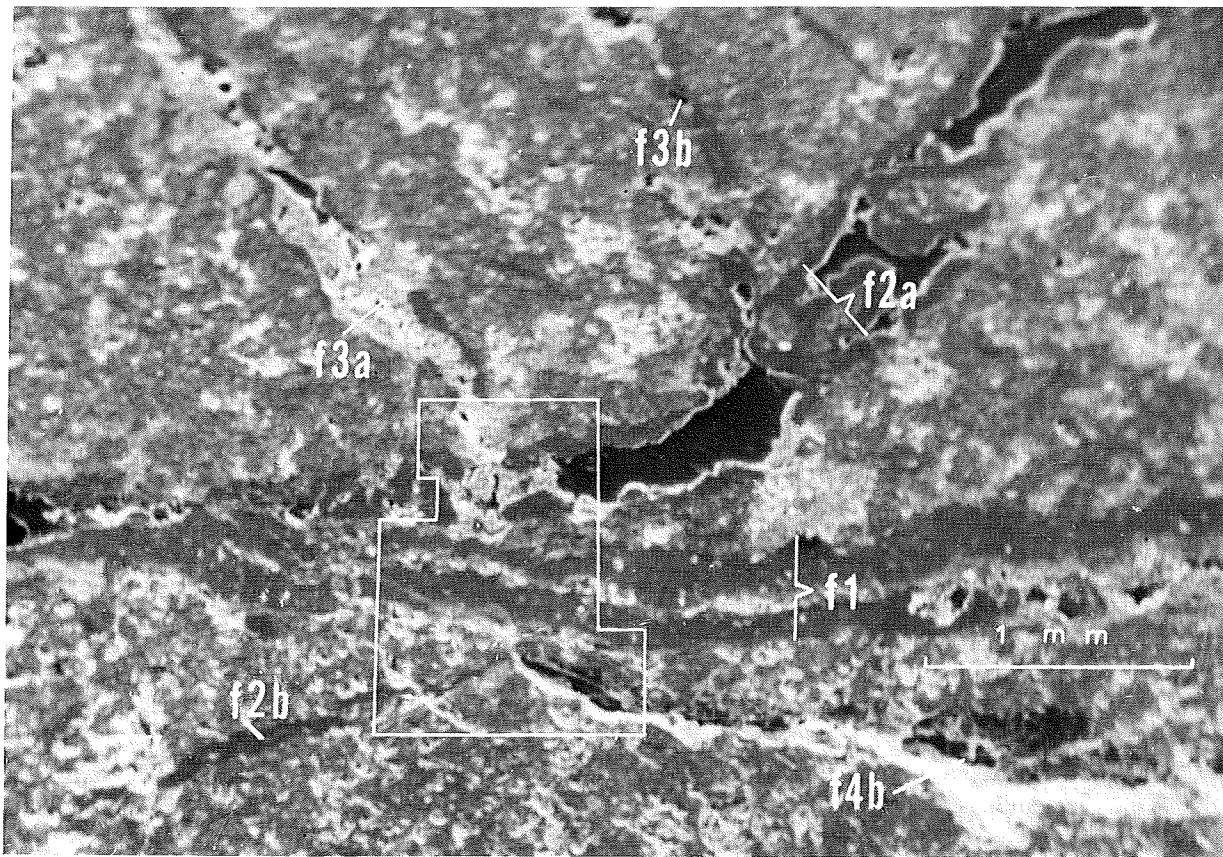

Plate 4. Sample RR 1132. SEM photomicrograph. $f1$ to $f4b$ = fractures (see text). See Plate 5 for enlargement of outlined portion.
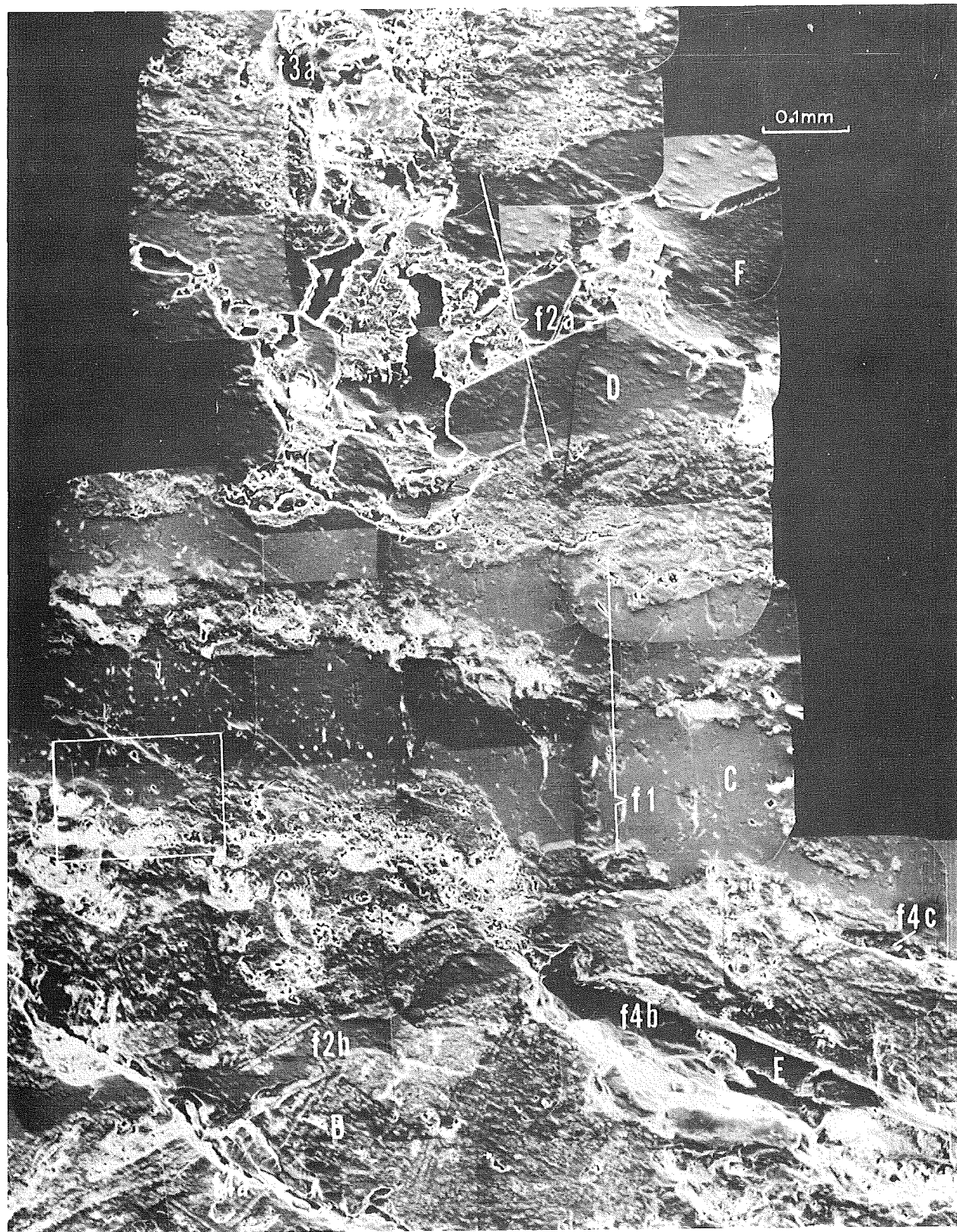
Plate 5. Sample RR 1132. SEM photomicrograph (mosaic). Enlargement of the outlined portion of Plate 4. B = calcite plates (?) in matrix; C = calcite; D = analcime; E = void; F = void now filled with epoxy; $f1$ to $f4c$ = fractures (see text). See Plate 6 for enlargement of outlined area.

the fracture walls. The sealing is complete except for a discontinuous chain of cavities at the center.

A second series of fracturing, *f2a*, angles down from the upper right-hand corner of Plate 4 to join *f1* at the center of the plate. Fracture *f2a* then continues toward the left, paralleling and crosscutting *f1*. Fracture *f2b* most likely occurred during the same fracturing episode that produced *f2a*. The evidence for this similarity in relative ages is that *f2a* and *f2b* trend in the same general direction, but are perpendicular to the later set of fractures, *f3a* and *f3b*. Fracture *f2b* is completely sealed with analcime, reflecting a change in the fluid chemistry from calcite to analcime supersaturation. Fracture *f2a* is lined with euhedral growths of analcime. The sealed and ingrown natures are clearly shown in Plate 5. Fractures *f3a* and *f3b* in Plate 4 oc-

curred next, propagating downward from the upper left until terminating on *f2a*. Fractures *f3a* and *f3b* are partially filled with analcime.

A more substantial change in the fluid chemistry is recorded in fractures *f4a, f4b,* and *f4c* of Plate 5. These cross-cut *f1* and *f2b*. Much of the lengths of *f4a, f4b,* and *f4c* are open cavities. They conspicuously narrow when cutting the analcime of *f2b*. Fracture *f4b* appears only as a "hollow" or shallow valley in Plate 6. This valley is paralleled by the more recent fracture *f5*. The fluids within *f4a, f4b,* and *f4c* have become undersaturated with respect to calcium carbonate. This undersaturation may be due to a number of things, including a decrease in fluid pH or fluid temperature. The undersaturation does not affect the analcime already deposited in *f2b* but causes large voids in the clayey matrix
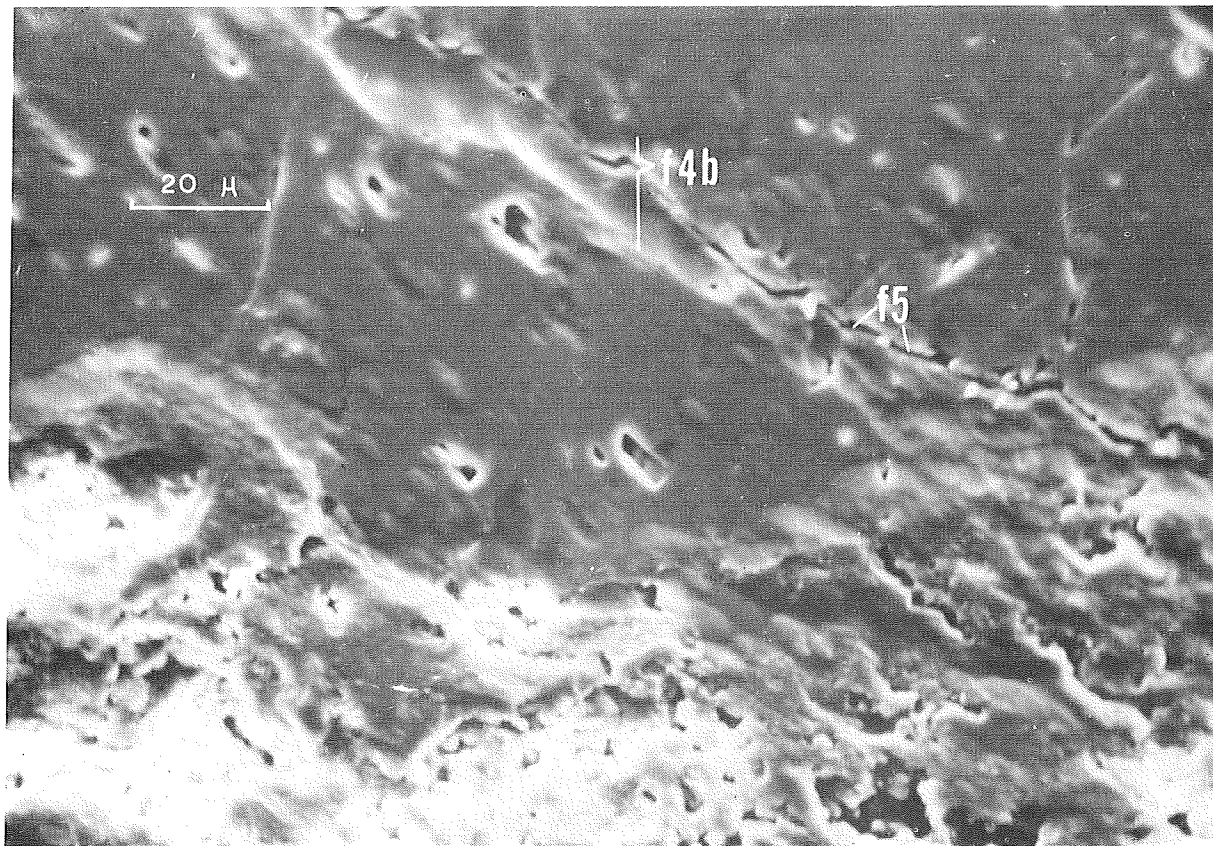

Plate 6. Sample RR 1132. SEM photomicrograph enlargement of a portion of Plate 5 (see text).
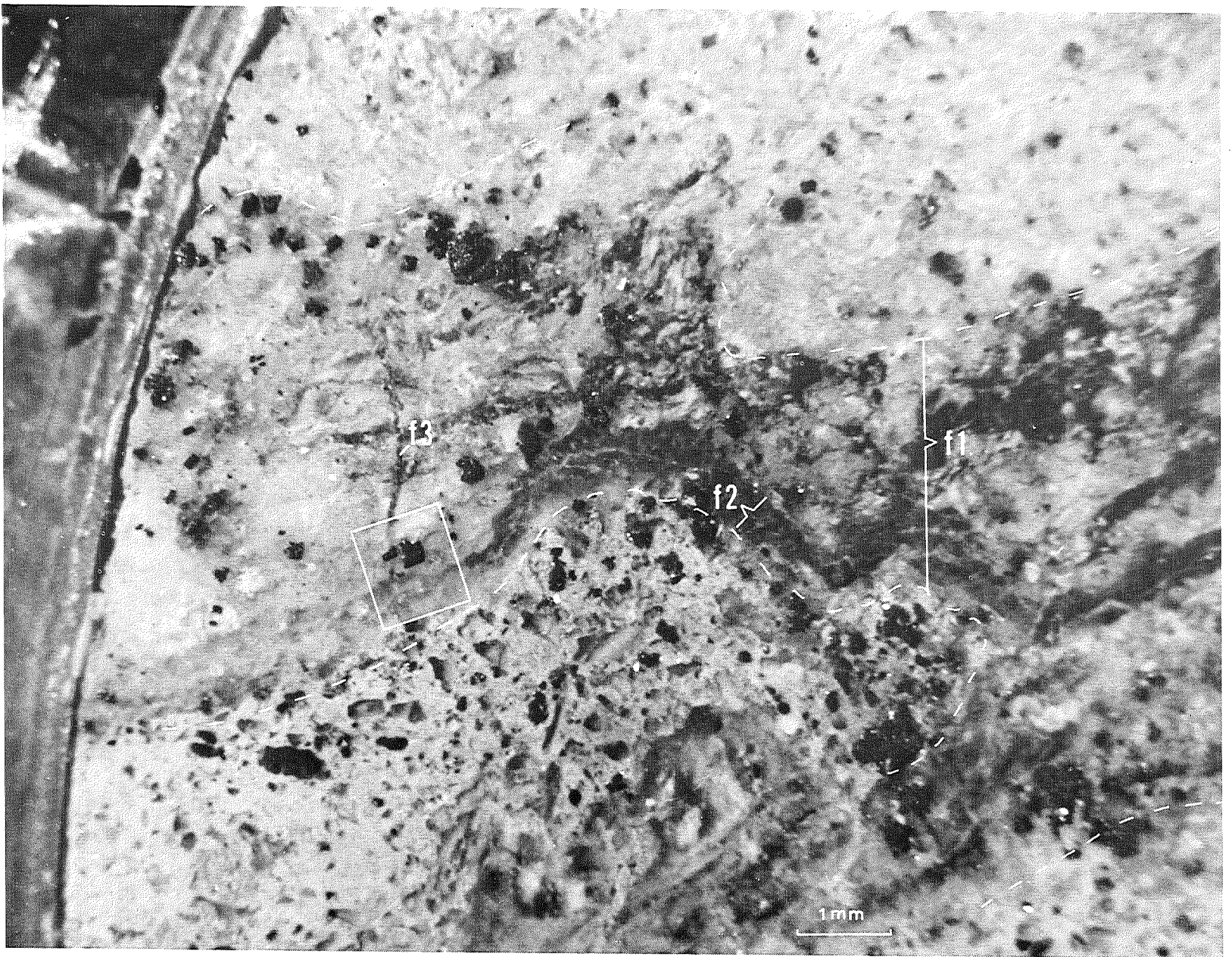
Plate 7. Sample RR 1107. Photomicrograph of an area of intersecting faulting and fracturing. Reflected light. (See text.) See Plate 8 for enlargement of outlined area.

by etching out any calcite cement. In Plate 6, fracture *f4b* is probably a zone of weakness in the calcite more readily attacked by the ion milling process. This zone may be due to the calcite "healing" across the fracture, or to a zone of lattice weakness due to the introduction of the undersaturated fluids. Fracture *f5* parallels this plane of weakness and may be due to drilling. This hollow is not due to the effects on ion milling on the open fracture *f5*.

In brief, the fracture history of rock sample RR 1132 is again one of repeated fracturing events superimposed on time-varying fluid chemistry. The fluid reactions usually involve fracture sealing. The fluid chemistry changes in time from calcite supersaturation to analcime supersaturation to calcite undersaturation. Pyrite crystals remain unaltered indicating continuous reducing conditions.

2.4 Sample RR 1107

Sample RR 1107 shows many sealed faults and fractures. Drag folding and offset bedding indicate at least 1 cm of movement along a faulted zone. The sealed faults and fractures form a boundary between well-indurated and poorly indurated regions of the sample. The sample is a gray-green, sandy claystone with siliceous and carbonate cement. Unaltered pyrite grains are present throughout the rock. Sample RR 1107 is very similar to sample RR 1132.

Sample RR 1107 is massively fractured and faulted in a narrow zone 3 mm wide. As can be seen in Plate 7, this fault zone (*f1*) consists of several wavy and broken bands. These bands consist of calcite and analcime. The wavy and broken texture is evidence for intermittent periods of calcite and analcime precipitation within fractures followed by further faulting and fracturing. The matrix surrounding fault *f1* contains many calcite and analcime shards. A later fracture, *f2*, along *f1*, marked the end of significant movement as is demonstrated by the sinuous and unbroken vein of analcime now filling *f2*.

Another episode of fracturing, *f3*, cross-cuts both *f1* and *f2*. A more detailed view of *f3* is shown in Plate 8. The mineralization within *f3* consists of both calcite and analcime and demonstrates the dependence of mineral precipitation on the micro- or local environment. Analcime fills *f3* where it crosses the analcime of *f2*. Calcite fills *f3* where it cuts the calcite-rich ma-

trix. In turn, *f5* is cross-cut by *f4*. Fracture *f4* is narrow, open, parallels *f1*, and extends down the center of *f2*.

Sample RR 1107 again exemplifies the episodic fracturing and sealing histories seen in both the Dunes and Raft River geothermal areas.

3. Fracture (crack) porosity

The flow of fluids through fractures depends, in part, on fracture porosity. Fracture or crack porosity can be determined through its effect on rock compressibility. We use differential strain analysis (DSA), a high-precision technique, to study the shape and spatial orientations of fractures [6]. Axial and radial linear differential strains were measured on each core sample.

The effects of fractures on the compressibility of rocks have been well documented. For a dry sample, the graph of strain versus pressure often shows two characteristic regions as in Fig. 5a. The "straight" portion of the curve at higher pressure (βP) is a result of the intrinsic compressibilities, β, of the constituent minerals. The increase of compressibility, represented by the "curved" portion of Fig. 5a, is due to crack closure. At the junction of these "curved" and "straight" portions, all fractures have closed. Walsh [9] demonstrated that the crack porosity, η_c in Fig. 5a, is the amount of volumetric strain between the origin and the zero pressure intercept of the "straight" portion (βP) of the stress-strain curve. Morlier [10] showed that the *distribution* of crack shapes could be obtained from the compression curves.

DSA is a new technique for measuring linear strain with a precision of 2×10^{-6} [6]. DSA is essentially the difference in linear strain between the sample and a fused silica standard exposed to the same high-pressure environment. The process of plotting differential strains transforms a curve such as the one in Fig. 5a to the form shown in Fig. 5b. In the transformation, the fracture porosity remains the strain between the origin and the zero pressure intercept of the "straight" intrinsic compressibility ($\beta'P$) portion of the DSA curve.

The precision of the DSA technique allows the fine structure of the linear stress-strain curves to be observed. Curves made up of straight line segments separated by discontinuities in slope, as in Fig. 5c, have been observed in some igneous samples. If the penny-shaped
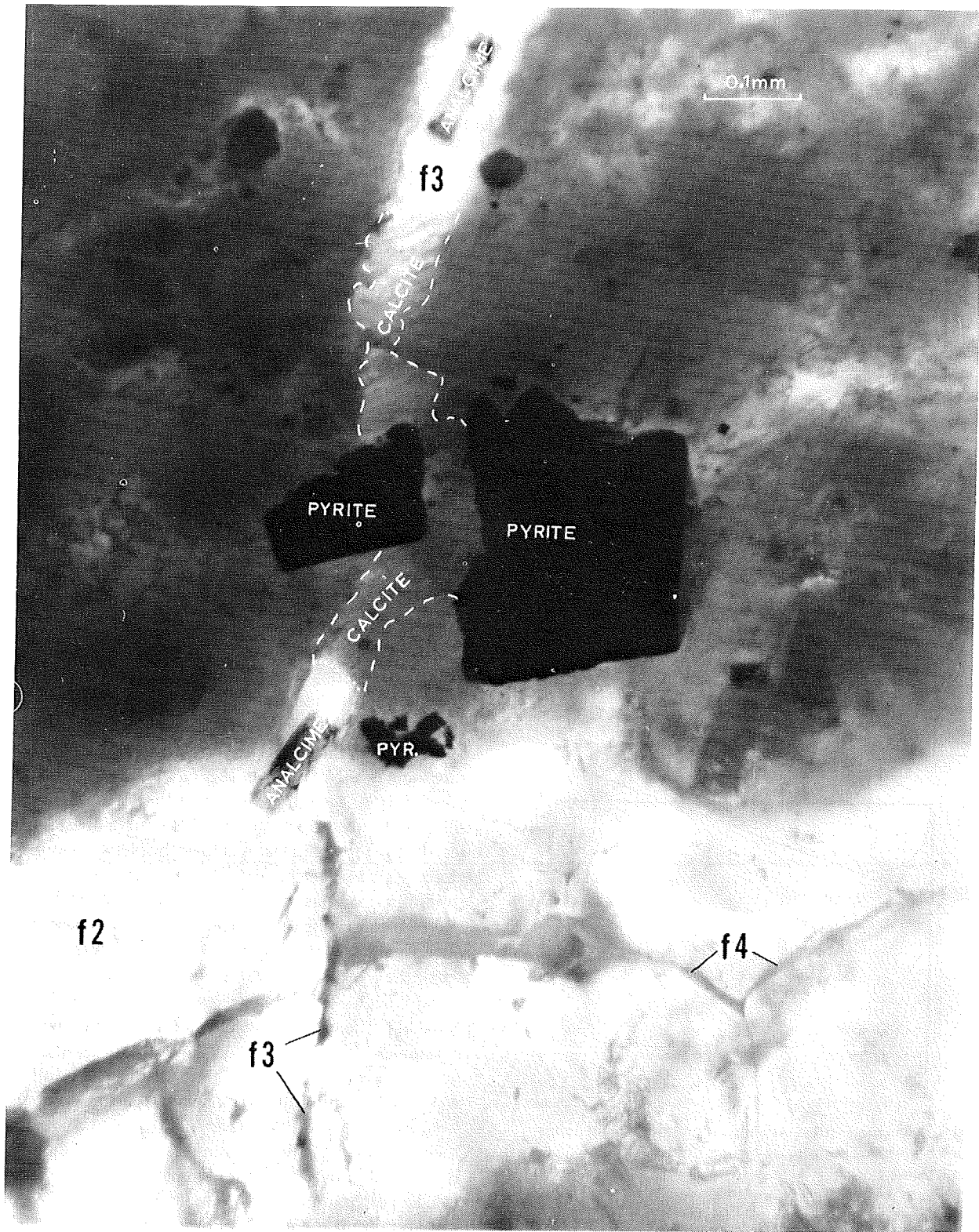
Plate 8. Sample RR 1107. Photomicrograph enlargement of a portion of Plate 7. Transmitted light (see text).
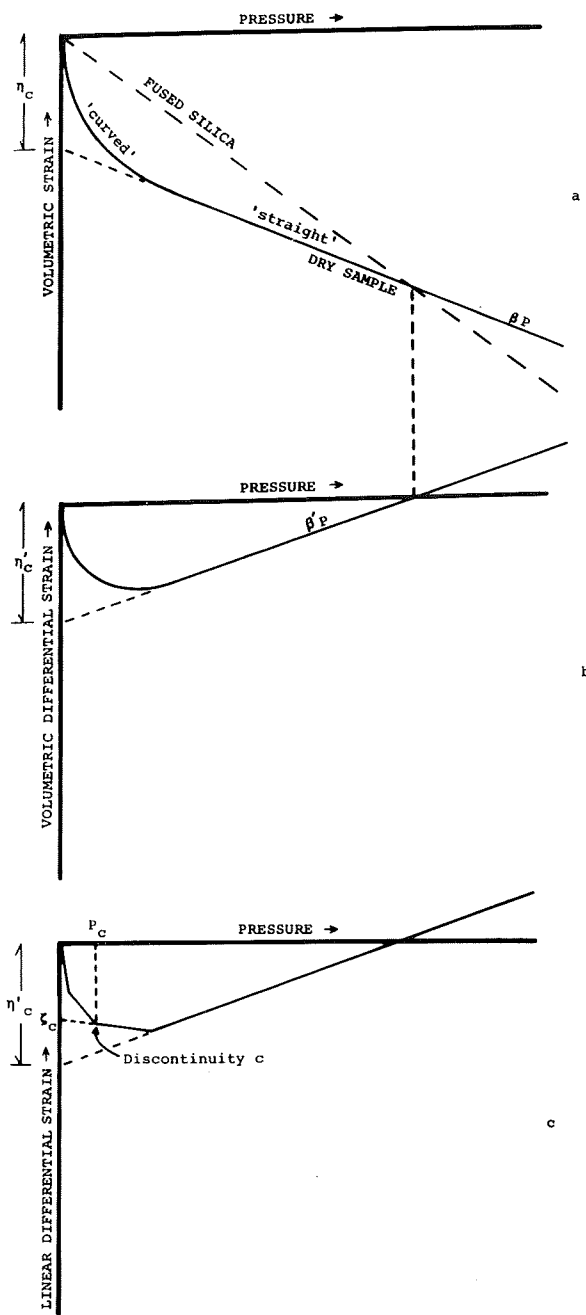
Fig. 5. Schematic stress–strain relationship. Symbol definitions: η_c = crack porosity, η'_c = linear differential strain due to fracture closure, P_c = pressure at closure discontinuity c, ζ_c = zero pressure intercept of linear segment beyond closure discontinuity c, β = compressibility, β' = differential compressibility, P = pressure. (a) Standard stress–strain curve. (b) Differential strain analysis (DSA) curve. (c) Segmented DSA curve.

crack model of Walsh [9] is used, then this segmented curve can be interpreted as being due to sharp peaks in the number of cracks with a particular aspect ratio (the ratio of width to length). Rocks with a continuous distribution of aspect ratios will have an appearance similar to Fig. 5b. In Fig. 5c, no cracks close completely over straight lined segments. At discontinuity c, all fractures with aspect ratio $\alpha = 4P_c (1 - \nu^2)/\pi E$ close, where ν and E are Poisson's ratio and Young's modulus respectively. This value of α is strongly dependent on the fracture model. To avoid this model-dependency, Simmons et al. [6] have used the experimentally determined values P_c and ζ_c as in Fig. 5c. P_c is the pressure at discontinuity c. ζ_c is the strain due to all the cracks that close *by* discontinuity c. The contribution to the total strain due to the fractures that close *at* discontinuity c is $\zeta_{c-1} - \zeta_c$. There exists a complete range of rocks that have a stress-strain curve such as Fig. 5c and those with one like Fig. 5b.

Previous experience in interpreting DSA data has been confined to dense, low-porosity, igneous rocks from the earth and to lunar samples. For the interpretation of DSA curves on sedimentary rocks, several modifications are needed. Compaction of rocks, particularly those rich in clay, results in a curve like that of Fig. 6a (note that strain is two orders of magnitude larger than the strain typical of igneous rocks). Initially, the rate of change of differential strain with pressure increases. Note that in Fig. 6a the intrinsic compressibility of the sample is greater than that of fused silica at all pressures so that the DSA curve does not recross the pressure axis. A similar, but less pronounced, effect occurs when the material is crushed in the vicinity of intergranular contacts. This effect may also occur due to the crushing of "bridges" or material spanning open fractures. Crushing appears as a downward offset of the DSA curve as shown in Fig. 6b. Crushing has also been observed in aggregates by Talwani and Nur [11]. The effect of small amounts of water within samples is shown in Fig. 6c. This effect was first noticed in igneous rocks [12] and may be the result of water movement in the crack network during compression. All of these effects are present to some degree in each of the Raft River area samples. Only "crushing" is observed in the Dunes area samples.

The preparation of DSA samples must be done with care to prevent the introduction of new fractures. Surfaces are cut parallel and perpendicular to the core
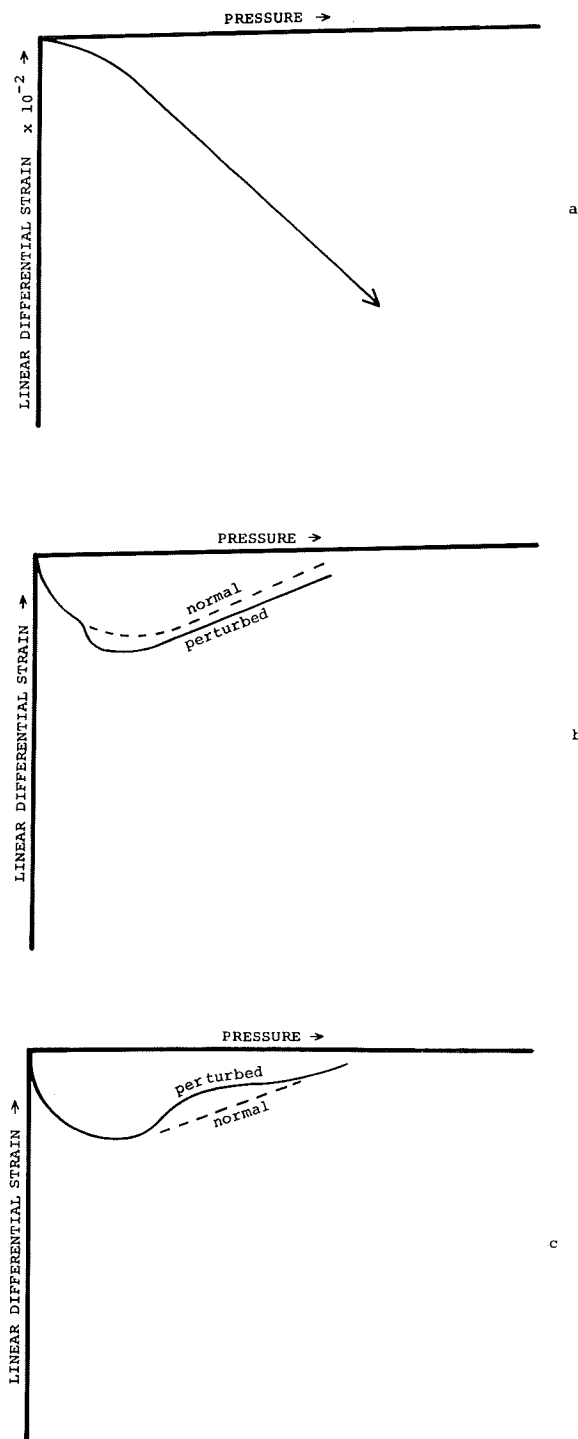
Fig. 6. Variations on a theme. (a) Effects of compaction; characteristic of clay-rich samples. (b) Effects of "crushing" (see text). (c) Effects of water.

axes and then ground. Samples are dried for 24 hours at room temperature and in a vacuum of less than 10^{-3} torr. For samples of low porosity, foil strain gages are attached directly to the sample with Tra-Con 2101 epoxy. The epoxy is allowed to cure completely. The sample is then encapsulated in Dow-Corning Sylgard to exclude the pressure medium. However, for highly porous rocks, both Sylgard and strain gages can be forced into pores under high pressures. The only method found to prevent entry into pores was a 1 mm thick coating of epoxy applied to the sample surface after drying but before further preparation.

Differential strain analyses were made on each sample. Strains were measured parallel (axial) and perpendicular (radial) to the core axis as a function of pressure to 2000 bars in increments ranging from 20 bars at low pressures to 100 bars at high pressures. The results are summarized in Table 1. Representative results for D 380, D 792, RR 1067, and RR 1107 will be described in detail.

3.1. Sample D 380

Sample D 380, described above, has several open, steeply dipping macroscopic fractures. The DSA curves, shown in Fig. 7, differ significantly in the radial and axial directions, an indication of strong anisotropy in physical properties. This anisotropy may be due to the preferred orientation of the fractures parallel to the core axis. The DSA results also indicate that not all the fractures are closed by 2000 bars.

For the radial direction, the DSA curve consists of four linear segments, each of which represents a specific crack shape. The results for the radial direction are shown in Table 1. The segment assumed to be the intrinsic compressibility curve was picked on the basis of only two points and has a large possible error. This "intrinsic" segment gives a minimum value of the differential strain due to total crack closure of $+162\mu$, where μ represents the factor 10^{-6}. The zero pressure residual differential is 18μ. For the axial direction, the DSA curve varies smoothly. By extrapolating the line defined by the last two points at high pressure, a minimum linear strain due to fracture closure of 183μ is obtained. There was no residual strain in the axial direction.

The DSA curves for axial and radial directions are quite different in both shape and values. The different

TABLE 1

Differential strain analysis results (errors in closure pressure are ±5 bars, in strain and fracture porosity are ±5% of the values reported)

Sample No.	Direction/ (location)/ [segment]		Closure pressure (bars)	Linear fracture strain (μ)	Total fracture porosity *	Remarks
D 380					0.0507%	
	radial	[1]	525	16		⎫
		[2]	1300	66		⎬ discrete dis **
		[3]	1840	80		⎭
	total			162		
	axial		1900?	183		continuous dis
D 495					0.0340%	initial grain crushing
	radial	[1]	1000	52		continuous dis
		[2]	1750	75		discrete dis
	total			127		
	axial	[1]	475	20		discrete dis
		[2]	1350	66		discrete dis
	total			86		
D 792					0.0371%	⎫
(see text)	radial	(X)	1600	135		⎪
		(YC)	1650	70		⎪
		(YE)	1750	94		⎬ continuous dis
	axial	(AC)	1700	166		⎪
		(AE)	1500	169		⎪
D 942					0.0392%	⎫
	radial		1400	106		⎬ continuous dis
	axial		1600	180		⎭
RR 1067					0.0610%	⎫
	radial		1350	220		⎪
	axial		600	170		⎬
RR 1132					0.0710%	⎪
	radial		700	210		⎭
	axial		900	290		
RR 1107						⎫
RR 1204						⎬ compaction effects
RR 1257						⎭ predominate

* Except for D 792, the total fracture porosity is based on the assumption of radial symmetry. Total fracture porosity then equals axial strain + 2 × radial strain.
** The abbreviation dis is used here for "distribution of crack closure pressures".

slopes at the higher pressures imply differences in the intrinsic compressibilities in these directions. The large differences in strain at each pressure imply that the cracks are anisotropically oriented.

The presence of linear segments in the compression curve for the radial direction and their absence for the axial direction are particularly interesting. The linear segments can occur only if no cracks close completely over the pressure range for each segment. However, the curves with continuously varying first derivatives can occur only if some cracks close completely at each pressure over the same range. If the spatial distribution
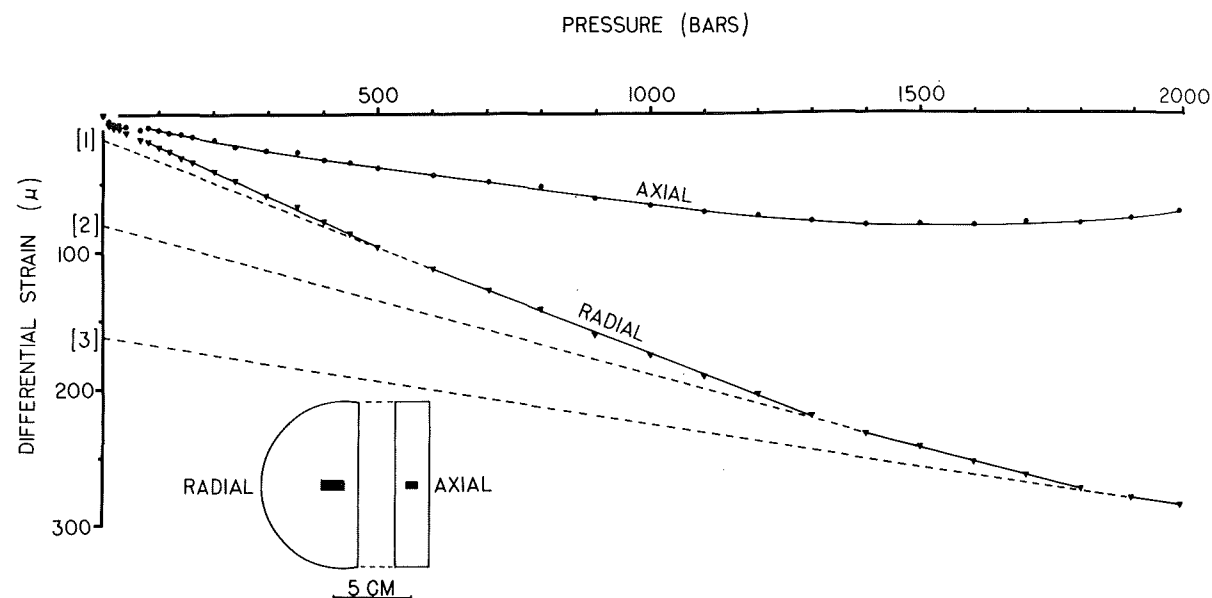
Fig. 7. Sample D 380, differential strain analysis. Sample size and shape is represented at lower portion of figure. The dark rectangles represent the size, position, and orientation of the strain gages.

of cracks in the sample is homogeneous, then lineal segments in one direction and curved segments in other directions can occur only if the sets of cracks with continuous distribution of closure pressures are normal to the directions in which the curved segments are measured. The set of cracks with a discrete distribution of closure pressures may be isotropically oriented. If we assume then that the DSA data in Fig. 7 fit such a model, then total crack porosity is twice the radial value plus the axial value, 0.0507%.

3.2. Sample D 792

DSA was performed for several directions and at several locations on sample D 792. The DSA curves and strain gage locations are shown in Fig. 8. This rock is a medium-grained, well-sorted sandstone showing no bedding. The sample has many steeply dipping fractures that apparently penetrate about 2 cm into the core. These fractures may have been caused by drilling. The upper boundary of the sample is formed by surfaces coated with fine adularia crystals.

The DSA curves on sample D 792 are smooth and show no straight segments within our experimental

error, about 2μ. Each curve shows some irregularities at low pressure. The irregularities are probably due to the "crushing effect". The DSA curve for the axial direction at the edge of the core (AE) parallels the curve for the axial direction at the center (AC), but is greater in magnitude by 50μ at higher pressures. The greater magnitude of strain at the edge is perhaps due to an increased number of fractures near the drilled surface. The stress due to drilling would tend to produce tensional cracks with surfaces perpendicular to the core axis. The total strain due to crack closures at 2000 bars for AC is $+166\mu$.

In the radial direction, strain was measured in two perpendicular directions x and y (see Fig. 8). The differential strain curves for the y direction at the center (YC) and edge (YE) differ only by 26μ at 2000 bars. The total strain at YC due to the closure of cracks at 2000 bars is 70μ. The differential strain for the x direction at the center (X) is greater in magnitude by 95μ than YC. This difference is not due to sample preparation and must be due to sample anisotropy. The differential strain at X due to crack closure is 135μ.

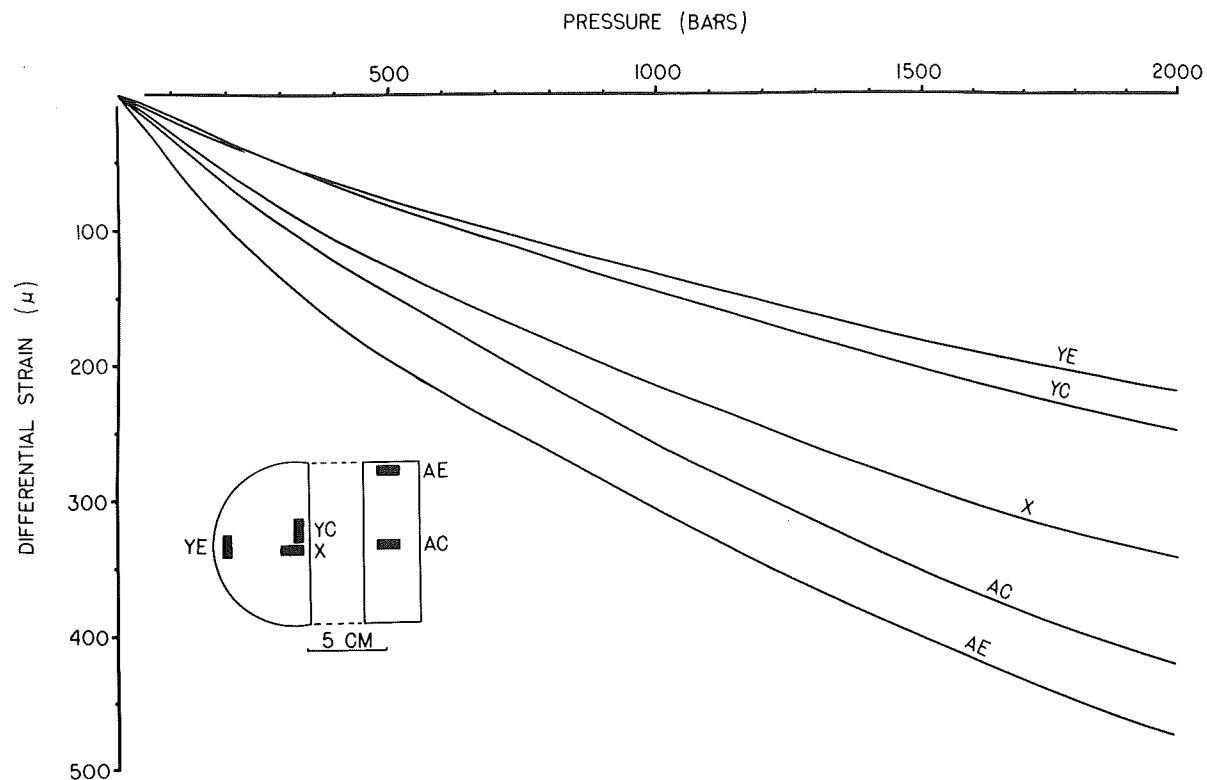The linear differential strains due to cracks in the three mutually perpendicular directions at the center

Fig. 8. Sample D 792, differential strain analysis. Data points have been omitted for clarity. Datum point location and scatter are similar to Fig. 7.

of the sample allow the calculation of the total crack porosity at the center. The total crack porosity is the sum of these linear strains, 0.0371%.

3.3. Sample RR 1067

Sample RR 1067 is a gray sandy claystone and is well indurated with siliceous and carbonate cement. Many fractures cross-cut the rock in apparently random directions. These fractures are filled with analcime and minor amounts of calcite. Several clay lenses cross the sample perpendicular to the core axis.

The DSA curves for sample RR 1067 are shown in Fig. 9. These curves consist of "curved" low-pressure portions and "straight" high-pressure portions. The curved portions require a continuous distribution of crack aspect ratios. Note, however, that the differential strains are much larger than in the Dunes area rocks. The compressibility for the axial direction in

sample RR 1067 is greater than that for the radial direction. The axial differential strain differs from the radial by 520μ at 2000 bars. Also, at high pressures, the axial curve is deflected downwards. This deflection is probably due to compaction and intergranular crushing. The strains due to crack closure in the axial and radial directions are 170μ and 220μ, respectively. This anisotropic behavior may be due to cracks introduced perpendicular to the core axis during the drilling process. The sample appears to possess radial symmetry. The total crack porosity is then 0.061%. At zero pressure, residual differential strains of 52μ and 44μ remained in the axial and radial directions, respectively.

3.4. Sample RR 1107

The DSA curves for sample RR 1107 are shown in Fig. 10. This sample exemplifies the effect on DSA curves of the compaction of a clay-rich rock. This effect
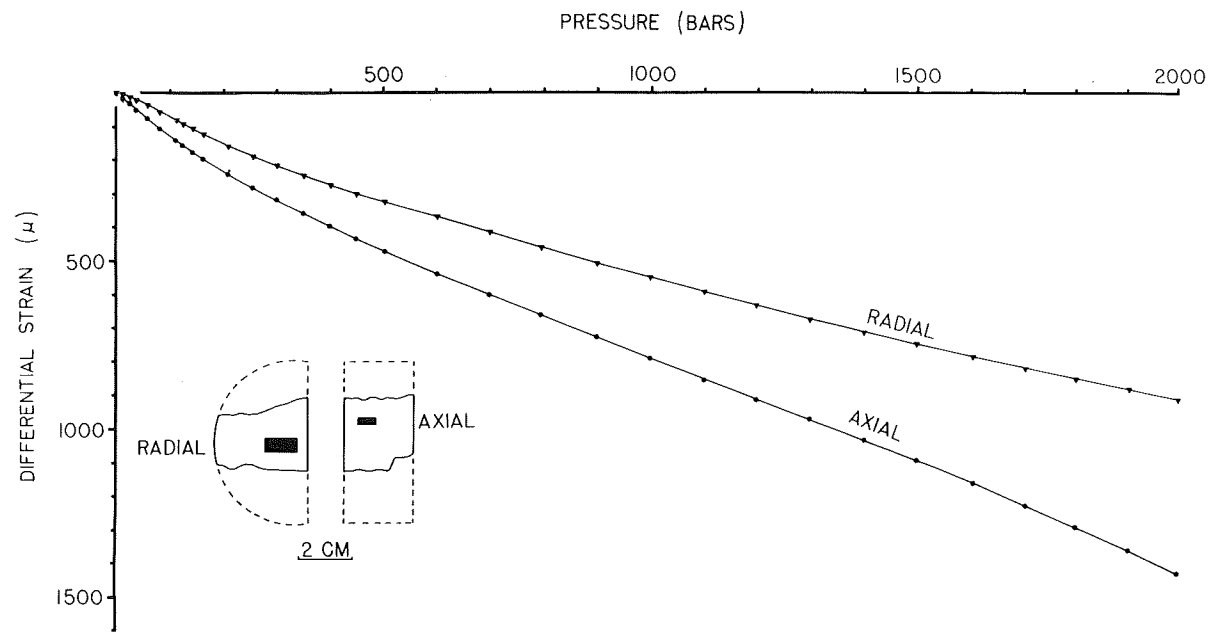
Fig. 9. Sample RR 1067, differential strain analysis.

makes the determination of fracture porosity impossible. The differential strain in the axial direction is much larger than in either the radial direction in this rock or in any other sample previously discussed. These DSA curves clearly show that bias in the data results when only well-indurated locations within the samples are used.

Sample RR 1107 shows a large change in compressibility over the 2000 bar pressure range. On an expanded scale similar to those of the previously described samples, the first portion of the DSA curve for
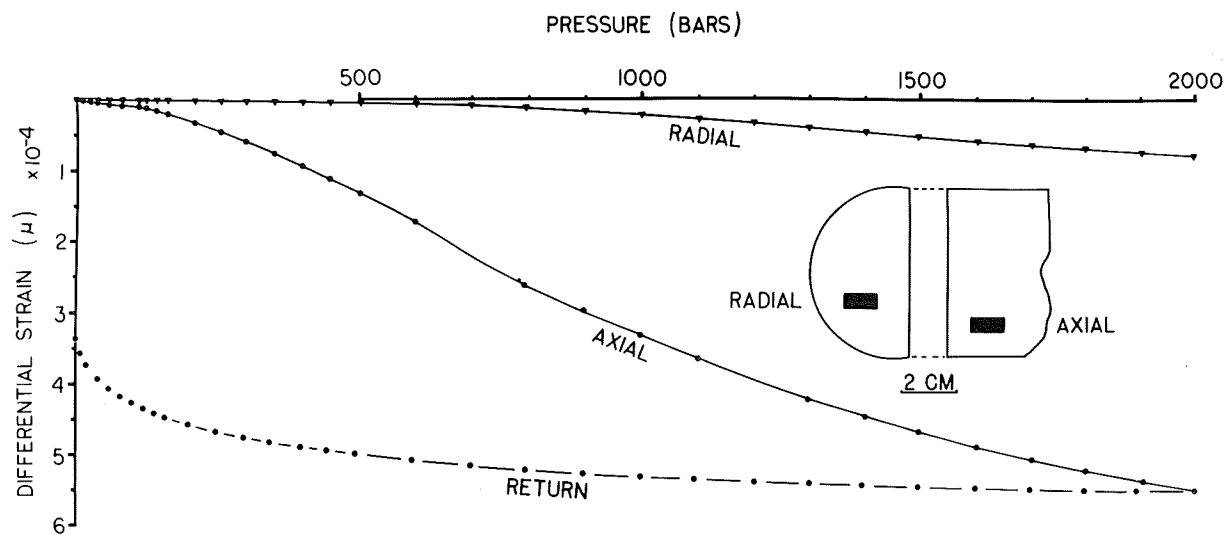

Fig. 10. Sample RR 1107, differential strain analysis.

the axial direction in sample RR 1107 looks similar to the curves of RR 1067. However, above 175 bars the compressibility becomes more than 60 times greater than the compressibility of any previously described sample. This large increase is probably due to the crushing and rotation of clays within the sample. The strain measurements during the return to zero pressure are shown to indicate how the sample is permanently affected. The maximum differential strain recorded is $56,000\mu$ at 2000 bars. The residual at zero pressure is $33,500\mu$. For an isotropic region, this strain would indicate a volumetric change of about 10% (indicating irreversible changes in the sample). The radial DSA curve for this sample is similar to the axial curve but much smaller in magnitude. The rock is strongly anisotropic and the results are dependent not only on the direction but also on the location where the measurements are made. As can be seen, the compaction effects of such poorly indurated clay-rich rocks completely obliterate the effects due to microfractures.

4. Conclusions

This preliminary study of cores from two geothermal areas demonstrates the potential of combined scanning electron microscopy, optical microscopy, and differential strain analysis for the study of geothermal areas.

The geothermal system involves the interplay among the fractures, rocks, and interstitial and fracture fluids. Both the Dunes and Raft River rocks show multiple periods of fracturing. Both areas had fluid chemistries that varied in time and usually resulted in fracture sealing. The two areas differ in their specific fracture mineralogy which is caused by the differences in bulk composition of the rocks. The feldspathic sandstones in the Dunes area develop quartz and adularia within fractures and interstitial areas. The clay-rich rocks of the Raft River area have interstitial and fracture minerals consisting mostly of calcite and analcime. Vertical variations in fracture mineralogy as well as the existence of impermeable shale beds indicate that lateral fluid movement is significant and may predominate.

Rock compressibilities indicate a low crack porosity even though large fractures are present in all samples. The low crack porosity is probably due to fracture sealing or fracturing being confined to a few large fractures. Fractures occur even in highly compactable clay-rich rocks. If drilling produces fractures, they are probably oriented with surfaces perpendicular to the core axis. Such drilling fractures apparently do not significantly increase the total fracture porosity. Fracturing and fracture sealing can alter the rock bulk physical properties greatly over distances as small as a few millimeters.

Due to the self-sealing nature of the geothermal system, geothermal areas will tend to develop dense impermeable cap rocks. Only the most recently formed fractures will remain open to fluid circulation. Sealed fractures can act as effective barriers to fluid movement through rocks. We speculate that fracture sealing will result in high heat flow and low electric resistivity only over regions of recent fracturing because new, open fractures conduct both fluids and electric currents.

Acknowledgments

References

1 W.A. Elders and D.K. Bird, Investigations of the Dunes geothermal anomaly, Imperial Valley, California, II. Petrological studies, presented at the International Symposium on Water-Rock Interaction of the International Union of Geochemistry and Cosmochemistry, Prague, (1974) 14 pp.

2 H.C. Helgeson, Geologic and thermodynamic characteristics of the Salton Sea geothermal system, Am. J. Sci. 266 (1968) 129.

3 G. Facca and F. Tonani, The self-sealing geothermal field, Bull. Volcanol. 30 (1967) 271.

4 J.W. Elder, Heat and Mass Transfer in the Earth: Hydrothermal Systems, N.Z. D.S.I.R. Bull. 169 (1966) 115 pp.

5 G. Simmons and D. Richter, Microcracks in rocks, in: The Physics and Chemistry of Rocks and Minerals, Proc. NATO Petrophysics Meeting (1976) in press.

6 G. Simmons, R.W. Siegfried and M. Feves, Differential strain analysis: a new method for examining cracks in rocks, J. Geophys. Res. 79 (1974) 4383.

7 G. Simmons, R. Siegfried and D. Richter, Characteristics of microcracks in lunar samples, Proc. Sixth Lunar Sci. Conf. 3 (1975) 3227.

8 H.L. Barnes and G.K. Czamanske, Solubilities and transport of ore minerals, in: Geochemistry of Hydrothermal Ore Deposits, ed. H.L. Barnes (Holt, Rinehart and Winston, New York, N.Y., (1967) 334.

9 J.B. Walsh, The effect of cracks on the compressibility of rocks, J. Geophys. Res. 70 (1965) 381.

10 P. Morlier, Description de l'état de fissuration d'une roche à partir d'essais non-destructifs simples, Rock Mech. 3 (1971) 125.

11 P. Talwani and A. Nur, Simultaneous measurements of velocity and compression of granular material (ABS), EOS 53 (1972) 527.

12 M. Feves and G. Simmons, Stress induced cracks in Westerly granite (ABS), EOS 56 (1975) 447.

13 E.G. Crosthwaite, H.R. Covington and S. Kluender, Raft River geothermal — intermediate hole No. 3, Unpublished stratigraphic section, U.S. Geological Survey, Denver (1974).